The triad interaction of ULK1, ATG13, and FIP200 is required for ULK complex formation and autophagy

Yutaro Hama[1,2,3], Yuko Fujioka[1], Hayashi Yamamoto[3,4], Noboru Mizushima[3], Nobuo N. Noda[1,2,*]

[1]Institute for Genetic Medicine, Hokkaido University, Sapporo 060-0815, Japan.
[2]Institute of Microbial Chemistry, Tokyo 141-0021, Japan.
[3]Department of Biochemistry and Molecular Biology, Graduate School of Medicine, The University of Tokyo, Tokyo 113-8655, Japan.
[4]Department of Molecular Oncology, Nippon Medical School, Institute for Advanced Medical Sciences, Tokyo 113-8602, Japan.
*Correspondence to Nobuo N. Noda: nn@igm.hokudai.ac.jp

Abstract

In mammals, autophagosome formation, a central event in autophagy, is initiated by the ULK complex comprising ULK1/2, FIP200, ATG13, and ATG101. However, the structural basis and mechanism of the ULK complex formation remain poorly understood. Here, we predicted the core interactions organizing the ULK complex using AlphaFold, which proposed that the intrinsically disordered region of ATG13 binds to the base of the two UBL domains in the FIP200 dimer using two phenylalanines and to the tandem MIT domain of ULK1, allowing for the 1:1:2 stoichiometry of the ULK1–ATG13–FIP200 complex. We confirmed the predicted interactions by point mutations and revealed the existence of direct triad interactions among ULK1, ATG13, and FIP200 in vitro and in cells, in which each interaction was additively important for autophagic flux. These results indicate that the ULK1–ATG13–FIP200 triadic interaction is crucial for autophagosome formation and provide a structural basis and insights into the regulation mechanism of autophagy initiation in mammals.

Introduction

Macroautophagy (hereafter autophagy) is an intracellular degradation system delivering cytoplasmic components to the lysosome via autophagosomes (Mizushima and Komatsu, 2011). Autophagy contributes to intracellular quality control by degrading defective proteins and organelles, such as polyubiquitinated proteins and damaged mitochondria. Alternatively, autophagy is induced by starvation as an adaptation mechanism. These physiological roles of autophagy are associated with various diseases, including cancer and neurodegenerative disorders (Mizushima and Levine, 2020). Therefore, understanding and controlling autophagy in clinical contexts is essential.

Autophagosome formation is performed by the evolutionally conserved autophagy-related (ATG) proteins, which form several functional units to act directly on autophagosome formation (Nakatogawa, 2020). Among them, the Atg1/ULK complex is critical in initiating autophagosome formation by organizing the formation site where all the functional units, such as ATG9 vesicles and ATG8 conjugation system, colocalize (Hama, Kurikawa et al., 2023; Kannangara, Poole et al., 2021; Kishi-Itakura, Koyama-Honda et al., 2014; Ren, Nguyen et al., 2023; Suzuki, Kirisako et al., 2001; Yamamoto, Kakuta et al., 2012; Zhou, Liu et al., 2021). In mammals, the ULK complex includes ULK1/2, ATG13, ATG101, and RB1CC1/FIP200 (Mizushima, 2010; Wong, Puente et al., 2013). Structural and functional analysis has made considerable progress in the yeast counterpart, the Atg1 complex, whose core comprises Atg1 (ULK1/2 homolog), Atg13, and Atg17 (remote homolog of FIP200) (Fujioka, Suzuki et al., 2014; Li, Chung et al., 2014; Lin and Hurley, 2016; Noda, 2024; Ragusa, Stanley et al., 2012). Crystallographic analyses have unveiled the detailed interaction mode of Atg13 with Atg1 and Atg17 and the mechanism of the Atg1 complex organization (Fujioka et al., 2014). Moreover, structure-based in vitro and in vivo functional analyses have revealed that the Atg1 complex undergoes liquid-liquid phase separation to organize the autophagosome formation site on the vacuolar membrane to initiate autophagy (Fujioka, Alam et al., 2020). However, structural and functional analyses of the mammalian ULK complex are considerably behind that of the yeast Atg1 complex, and structural information on the interactions comprising the core of the ULK complex has been limited to low-resolution electron microscopy (EM) data (Shi, Yokom et al., 2020). Recently, calcium transients on the endoplasmic reticulum surface were proposed to trigger the liquid-liquid phase separation of FIP200 to organize the autophagosome formation site, thereby initiating autophagy (Zheng, Chen et al., 2022). However, the lack of structural information makes elucidating the molecular mechanisms underlying these events challenging.

This study predicted the structure of the ULK1–ATG13–FIP200 complex using the

AlphaFold2 multimer (Evans, O'Neill et al., 2021), which unveiled the detailed interactions between ATG13 and FIP200, ATG13 and ULK1, and ULK1 and FIP200. In vitro and in vivo mutational analysis confirmed all the predicted interactions, which were demonstrated to be important for autophagy. Furthermore, we found that the FIP200–ATG13 and ULK1–ATG13 interactions partially complement each other for the autophagy initiation. These findings establish the mechanism of ULK complex formation and provide a structural basis for understanding the ULK complex phase separation and regulation mechanism of autophagy in the mammalian context.

Results

Structural prediction of the ULK1–ATG13–FIP200 complex identifies FIP200-interacting residues in ATG13

Previous studies reported that the C-terminal region of ULK1 and the C-terminal intrinsically disordered region of ATG13 bind to the N-terminal region of the FIP200 homodimer (Alers, Loffler et al., 2011; Ganley, Lam du et al., 2009; Hieke, Loffler et al., 2015; Hosokawa, Hara et al., 2009; Jung, Jun et al., 2009; Papinski and Kraft, 2016; Wallot-Hieke, Verma et al., 2018). However, structural details of the interactions forming the ULK complex remain elusive. To understand the mechanism of the ULK complex formation, we predicted the structure of the FIP200 [1–634 amino acids (aa)] dimer complexed with ATG13 (isoform c, 363–517 aa) and ULK1 (801–1,050 aa) by AlphaFold2 with the AlphaFold-Multimer option (Fig. 1A, Fig. S1). For clarity, flexible loop regions in FIP200 with low pLDDT scores were removed from Figure 1A. The overall structure is consistent with the low-resolution cryo-EM model reported previously (Shi et al., 2020), including the C-shape of the FIP200 dimer and the binding of ATG13 and ULK1 to the FIP200 dimer one by one, resulting in the 1:1:2 stoichiometry of the ULK1–ATG13–FIP200 complex. The two FIP200 molecules are named $FIP200^{A}$ and $FIP200^{B}$, where $FIP200^{A}$ is the one close to ULK1. Wide interactions were predicted between the four molecules, with a buried surface area of 3,658 $Å^2$ for $FIP200^{A}$–$FIP200^{B}$, 2,195 $Å^2$ for $FIP200^{A}$–ATG13, 1,966 $Å^2$ for $FIP200^{B}$–ATG13, 2,140 $Å^2$ for ATG13–ULK1, and 1,681 $Å^2$ for $FIP200^{A}$–ULK1. No interaction was observed between $FIP200^{B}$ and ULK1.

One ATG13 molecule binds to the FIP200 dimer through the interaction of residues 365–398 and 394–482 with $FIP200^{B}$ and $FIP200^{A}$, respectively, resulting in a 1:2 stoichiometry of the ATG13–FIP200 complex. Previous studies using hydrogen-deuterium exchange coupled to mass spectrometry identified three regions (M1–M3) in ATG13 responsible for FIP200 binding (Shi et al., 2020). Among these sites, the side-chain of Phe377 in M1, Phe397 in M2, and Phe453 in M3, was deeply inserted into the hydrophobic pockets of FIP200 (Fig. 1B). Direct interaction between FIP200 (1–634) and Atg13 (363–517)

was confirmed by isothermal titration calorimetry (ITC) with a Kd value of 6.6 μM, which was severely attenuated by alanine substitution at these three phenylalanine sites (F377A, F394A, F453A; FIP3A) (Fig. 1C, Fig. S2). Furthermore, the *ATG13*^{FIP3A} mutant expressed in *atg13* KO cells displayed a significantly reduced coprecipitation rate of the endogenous FIP200 (Fig. 1D, E). These results confirm that ATG13 and FIP200 interact with each other via the residues predicted by AlphaFold2 in vitro and in vivo.

ULK1 and ATG13 interact via MIT-MIM interaction similar to yeast Atg1–Atg13

Next, we focused on the interaction between ULK1 and ATG13. We previously determined the crystal structure of the yeast Atg1–Atg13 complex, which revealed that the tandem two microtubule-interacting and transport (MIT) domains in Atg1 bind to the tandem two MIT-interacting motifs (MIMs) of ATG13 (Fig. 2A, right) (Fujioka et al., 2014). The predicted structure of the ULK1–ATG13 complex was quite similar to that of the yeast Atg1–Atg13 complex and was constructed by the ULK1^{MIT1}–ATG13$^{MIM(C)}$ and ULK1^{MIT2}–ATG13$^{MIM(N)}$ interactions (Fig. 2A, left). According to the predicted structure, Phe470 of ATG13$^{MIM(N)}$ and Phe512 of ATG13$^{MIM(C)}$ were inserted into the hydrophobic pocket of ULK1^{MIT2} and ULK1^{MIT1}, respectively (Fig. 2B). Direct interaction between ULK1 (636–1,050) and Atg13 (363–517) was confirmed by ITC with a Kd value of 0.34 μM, which was severely attenuated by alanine substitution at these two phenylalanine sites (F470A, F512A; ULK2A) (Fig. 2C, Fig. S2). In *atg13* KO cells, the ULK1 expression level was significantly reduced, suggesting that the lack of ATG13 severely destabilized ULK1. The exogenous expression of *ATG13*^{WT}, but not of the *ATG13*^{ULK2A} mutant, rescued the endogenous ULK1 expression (Fig. 2D, E). This result suggests that the *ULK2A* mutation in ATG13 attenuates the ATG13–ULK1 interaction, including in vivo. These results confirm that ATG13 and ULK1 interact via the residues predicted by AlphaFold2 in vitro and in vivo.

Direct interaction between ULK1 and FIP200 is essential for autophagy

Although AlphaFold2 predicted the direct interaction between ULK1 and FIP200 over a reasonably large contact area (1681 Å^2) (Fig. 3A), a previous study reported that ULK1 required ATG13–ATG101 for FIP200 binding in vitro (Shi et al., 2020). In our predicted structure, ULK1^{MIT1} and ULK1^{MIT2} interact directly with FIP200, with the Leu967 of ULK1^{MIT1} and Phe997 of ULK1^{MIT2} inserted on the hydrophobic groove of FIP200 (Fig. 3A, B). Although we failed to measure the affinity between ULK1 and FIP200 by ITC due to aggregation upon their mixing, an in vitro pull-down assay indicated that ULK1 directly interacted with FIP200, which was significantly attenuated by the FIP2A (L967A, F997A) mutation (Fig. 3C, D). Consistently, the ULK1^{FIP2A} mutant lost the interaction with FIP200 while partially retaining

the interaction with ATG13 in cells (Fig. 3E, F). These results confirm the direct ULK1–FIP200 interaction in vitro and in vivo. Our results establish the mode of the three independent interactions, ATG13–FIP200, ATG13–ULK1, and ULK1–FIP200, in the ULK complex.

To investigate the physiological importance of the ULK1–FIP200 interaction, we assessed autophagy flux using the Halo-LC3 processing assay (Rudinskiy, Bergmann et al., 2022; Yim, Yamamoto et al., 2022). *Ulk1,2* DKO mouse embryonic fibroblasts (MEFs) expressing FLAG-tagged wild-type ULK1 produce a stronger band of cleaved Halo than cells which do not express ULK1. The intensity of this cleaved Halo band corresponds to the amount of Halo-LC3 delivered to lysosomes in an autophagy-dependent manner. *Ulk1,2* DKO MEFs expressing the ULK1^{FIP2A} mutant had partially but significantly reduced processed Halo bands upon starvation compared to ULK1^{WT}-expressing cells, confirming that the direct ULK1–FIP200 interaction is crucial, although partially, for autophagy activity (Fig. 3G, H). This partial phenotype would be due to an indirect interaction between ULK1 and FIP200 via ATG13, which was supported by the observation that the ULK1^{FIP2A} mutant colocalized with FIP200 in cells, although less efficiently than ULK1^{WT} (Fig. 3I).

Triadic ULK1–ATG13–FIP200 interactions are critical for autophagic flux

We compared the autophagic flux of impaired ATG13–ULK1 and ATG13–FIP200 interactions to confirm the hypothesis that indirect triadic complexes are functional for autophagy. We generated knock-in (KI) cell lines that included *ATG13^{FIP3A}*, *ATG13^{ULK2A}*, and *ATG13^{FU5A}* (F377A, F394A, F453A, F470A, F510A; FU5A) followed by a 3xFLAG-tag in the genomic *ATG13* locus of HeLa cells (Fig. 4A, B). Since overexpressed *ATG13-FLAG* is more than 20-fold higher than its endogenous level, the mutation significance can be evaluated at more physiological expression levels using the KI cell lines (Fig. S3). The ATG13^{FIP3A} and ATG13^{ULK2A} mutants displayed partial colocalization with FIP200, whereas the ATG13^{FU5A} mutant displayed scarce colocalization with FIP200 (Fig. 4C). Next, we expressed *Halo-LC3* in these KI cells and performed a Halo processing assay. Cleaved Halo was partially reduced in ATG13^{FIP3A} and ATG13^{ULK2A} cells compared to ATG13^{WT} cells. In contrast, cleaved Halo in ATG13^{FU5A} cells was almost equivalent to that in the knock-out cells (Fig. 4D, E). These results suggest that ATG13–ULK1 and ATG13–FIP200 bindings complement each other in autophagy function and that ULK1, ATG13, and FIP200 directly bind to each other to organize the robust ULK complex.

Discussion

The interaction mechanism of ULK1–ATG13–FIP200, the core of the ULK complex, has been

extensively studied (Alers et al., 2011; Ganley et al., 2009; Hieke et al., 2015; Hosokawa et al., 2009; Jung et al., 2009; Papinski and Kraft, 2016; Shi et al., 2020). However, most of these studies were not based on structural information, and the knowledge of the interaction mechanism remained limited. Notably, the evidence for ULK1–FIP200 interaction has been limited to in vitro studies (Shi et al., 2020), and its physiological significance has not been characterized. In this study, AlphaFold2-based point mutational analysis provides solid evidence for the direct ULK1–ATG13, ATG13–FIP200, and ULK1–FIP200 bindings in vitro and in vivo. Additionally, the triadic interaction is complementary in the cell.

One major structural difference between the mammalian ULK complex we predicted here and the yeast Atg1 complex is that one ATG13 binds to two FIP200s within the same FIP200 dimer in mammals, whereas one Atg13 binds to two Atg17s in the distinct Atg17 dimers in yeast (Fig. 4F). The latter binding mode of Atg13 bridges Atg17 dimers to each other to form a higher-order assemblage (Yamamoto, Fujioka et al., 2016), which is considered to be the Atg1 complex's phase separation mechanism (Fujioka et al., 2020). Conversely, ATG13 cannot bridge FIP200 dimers to each other and thus cannot induce a higher-order assemblage of the ULK complex, which necessitates another mechanism for phase separation. A recent study reported that calcium transients on the endoplasmic reticulum surface trigger FIP200 phase separation (Zheng et al., 2022); however, the detailed mechanisms are unresolved. Further studies are required to elucidate the mechanisms of phase separation in organizing the autophagosome formation sites in mammals.

In addition to Atg17, budding and fission yeasts have Atg11 as a closer homolog of FIP200 (Kim, Kamada et al., 2001; Li et al., 2014; Pan, Shao et al., 2020; Sun, Li et al., 2013; Yorimitsu and Klionsky, 2005). Atg11 and Atg17 interact with Atg1 and Atg13, respectively, whereas Atg11–Atg13 and Atg17–Atg1 interactions have not been reported. *Arabidopsis thaliana*, which belongs to the Archaeplastida group, a supergroup distant from Opisthokonta (including yeasts and mammals), also has Atg1, Atg13, and Atg11 (Burki, Roger et al., 2020; Li et al., 2014). The *A. thaliana* Atg11 interacts with Atg13 but not with Atg1 (Li et al., 2014). The triadic interaction of Atg1/ULK1, ATG13, and Atg11/Atg17/FIP200 has not been reported for any species other than mammals. This triadic interaction is likely beneficial for cells that form the complicated cellular communities that comprise the metazoans. The most likely physiological significance is the fine-tuning of tissue-specific autophagic activity. Consistent with this idea, several splicing variants of ATG13 are present in vertebrates (Alers, Wesselborg et al., 2014; Hieke et al., 2015; Jung et al., 2009). In humans, at least five splicing variants are known, including the isoform 3 lacking the C-terminal ULK1-binding site (MIMs, Fig. 2A) (Alers et al., 2014; Jung et al., 2009). The avian Atg13 has seven splicing variants, some lacking parts of the FIP200 interaction site (Alers et al., 2014; Hieke et al., 2015). This

study found that a single disruption of the FIP200–ATG13 or ULK1–ATG13 interaction results in a partial reduction of autophagy activity (Fig. 4D). In the individual context, the tissue- and organ-specific fine-tuning of the autophagy activity may occur by regulating the expression amount and ratio of splicing variants that lack some of the triad interactions. Generating KI mice with the point mutations identified in this study might help investigate the significance of the triadic binding at the individual level.

Materials and Methods

Cell culture

HeLa cells and MEFs were cultured in Dulbecco's Modified Eagle medium (DMEM) (043-30085; Fujifilm Wako Pure Chemical Corporation) supplemented with 10% fetal bovine serum (FBS) (172012; Sigma-Aldrich) in a 5% CO_2 incubator at 37°C. Cells were washed twice with phosphate-buffered saline (PBS) and incubated in amino acid-free DMEM (048-33575; Fujifilm Wako Pure Chemical Corporation) without FBS for starvation. *atg13* KO HeLa cells (Hama et al., 2023) and *Ulk1 Ulk2* double knockout MEFs (Cheong, Lindsten et al., 2011) were described previously.

Plasmids for mammalian cells

Plasmids for stable expression were generated as follows: DNA fragments encoding human ULK1 (NM_003565.4) and ATG13 (Hosokawa et al., 2009) were inserted into the retroviral plasmid pMRX-IP (puromycin-resistant marker) (Kitamura, Koshino et al., 2003; Saitoh, Nakayama et al., 2003) with a 3 × FLAG epitope tag. Site-directed mutagenesis was used to introduce ATG13 FIP3A, ATG13 ULK2A, ATG13 FU5A, and ULK1 FIP2A mutations. pMRXIB-ratLC3B was described previously (Yim et al., 2022). Plasmids for *ATG13* KI were generated as follows: sgRNAs targeting the exon 14 of *ATG13* (5′-GGCCTCCCCTCACGATGTCT-3′) were inserted into the *Bpi*I site of PX458 [pSpCas9(BB)-2A-GFP; Addgene #48138]. Donor plasmids for *ATG13* KI were generated as follows: 500 base-pair (bp) and 682 bp homology arms were amplified from the genomic *ATG13* locus around exon 14 and inserted to flank the KI cassettes (described in Fig. 4A) in the donor plasmid (pKnockIn). The coding sequence of 3xFLAG-tagged ATG13 with or without FIP3A, ULK2A, or FU5A mutations was amplified from stable expression plasmids (described above) and inserted just behind the 5' homology arm.

Stable expression in HeLa cells by retroviral infection

HEK293T cells were transfected with the retroviral plasmid with pCG-gag-pol and pCG-VSV-G (a gift from Dr. T. Yasui, National Institutes of Biomedical Innovation, Health and Nutrition)

using FuGENE HD (E2311; Promega) for 4 h in Opti-MEM (31985-070; Gibco). After cell cultivation for 2 days in DMEM, the retrovirus-containing medium was harvested, filtered through a 0.45-μm filter unit (Ultrafree-MC; Millipore), and added to HeLa cells or MEFs with 8 μg/ml polybrene (H9268; Sigma-Aldrich). After 24 h, 2 μg/ml puromycin (P8833; Sigma-Aldrich) or 2.5 μg/ml blasticidin (022-18713; Fujifilm Wako Pure Chemical Corporation) were used to select the stable transformants.

Plasmids for protein preparation

To construct the expression plasmid encoding an N-terminal maltose binding protein (MBP) followed by an HRV3C protease site, the genes were amplified by PCR and cloned into the pET15b vector. The genes were amplified by PCR and cloned into the pET15b-MBP vector for the plasmids encoding N-terminal MBP-tagged ULK1, ATG13, and FIP200. Similarly, for the plasmids encoding N-terminal glutathione S-transferase (GST)-tagged ULK1, the genes were amplified by PCR and cloned into the pGEX6p-1 vector. The NEBuilder HiFi DNA Assembly Master Mix (New England BioLabs) was used to assemble the PCR fragments. PCR-mediated site-directed mutagenesis was used to introduce the mutations that led to the specified amino acid substitutions. All constructs were sequenced to confirm their identities.

Protein expression and purification

E. coli BL21 (DE3) cells were used to express all recombinant proteins. After cell lysis, MBP-FIP200 (1–634) was purified by affinity chromatography using Amylose Resin High Flow (New England Biolabs). Next, MBP was cleaved with the human rhinovirus 3C protease. The eluates were then desalted with 20 mM Tris-HCl, pH 8.0, and 150 mM NaCl utilizing a Bio-Scale Mini Bio-Gel P-6 desalting column (Bio-Rad Laboratories). Subsequently, the cleaved MBP was removed by reappliying FIP200 (1–634) to an Amylose Resin High Flow column. For the pull-down assay, MBP-FIP200 (1–634) eluted from the amylose resin continued to be purified on a HiLoad 26/60 Superdex 200 PG column eluted with 20 mM Tris-HCl, pH 8.0, and 150 mM NaCl.

Affinity chromatography with Amylose Resin High Flow (New England Biolabs) was used to purify the MBP-Atg13 (363–517) and MBP-ULK1 (636–1,050) proteins. They were further purified on a HiLoad 26/60 Superdex 200 PG column and eluted with a buffer containing 20 mM Tris-HCl, pH 8.0, and 150 mM NaCl. Similarly, GST-ULK1 (636–1050) underwent initial purification using a GST-accept resin (Nacalai Tesque, 09277-14). This step was followed by further purification on a HiLoad 26/60 Superdex 200 PG column using the same elution buffer as above.

In vitro pull-down assay

Purified proteins were incubated with GST-accept beads (Nacalai Tesque) at 4°C for 30 min. The beads were washed three times with PBS, and proteins were eluted with 10 mM glutathione in 50 mM Tris-HCl (pH 8.0). SDS-PAGE was used to separate the samples, and protein bands were detected by One Step CBB (BIO CRAFT).

Isothermal titration calorimetry

The binding of FIP200 (1–634) to MBP-ATG13 (363–517) and MBP-ATG13 (363–517) to MBP-ULK1 (636–1,050) was measured by ITC, with a MICROCAL PEAQ-ITC calorimeter (Malvern) and stirring at 750 rpm at 25°C. All proteins were prepared in a solution of 20 mM Tris-HCl, pH 8.0, and 150 mM NaCl. The titration of MBP-ATG13 (363–517) with FIP200 (1–634) involved 18 injections of 2 μl of the MBP-ATG13 (363–517) solution (229 μM) at 150 s intervals into a sample cell containing 300 μl of FIP200 (1–634) (4 μM). The titration of MBP-ULK1 (636–1,050) with MBP-ATG13 (363–517) involved 18 injections of 2 μl of the MBP-ULK1 (636–1,050) solution (232 μM) at 150 s intervals into a sample cell containing 300 μl of MBP-ATG13 (363–517) (22.9 μM). The isotherm was integrated and fitted with the one-side-binding model of the Malvern MicroCal PEAQ-ITC analysis software. The error of each parameter indicates the fitting error.

Generation of KI cell lines

HeLa cells were transfected with the PX458-based plasmid expressing sgRNA for the *ATG13* gene and donor plasmids using FuGENE HD (E2311; Promega). One day after transfection, the KI cells were selected with 1 mg/mL G418 for 14 days. After single clones were isolated, clones positive for the FLAG tag and negative for wild-type ATG13 were screened by immunoblotting.

Preparation of whole cell lysates and immunoblotting

HeLa cells were lysed with 0.2% n-octyl-β-D-dodecyl maltoside in lysis buffer [50 mM Tris-HCl (pH 7.5), 150 mM NaCl, 1 mM EDTA, EDTA-free protease inhibitor cocktail (04080; Nacalai Tesque)] for 15 min on ice. After centrifugation at 20,000 × g for 15 min at 4°C, the supernatants were mixed with 20% volumes of 6 × SDS-PAGE sample buffer. The samples were subjected to SDS-PAGE and transferred to Immobilon-P PVDF membranes (IPVH00010; EMD Millipore). The primary antibodies used for immunoblotting were rabbit polyclonal antibodies against FIP200 (17250-1-AP; ProteinTech), ATG13 (13273; Cell Signaling), and ULK1 (8054; Cell Signaling) and mouse monoclonal antibody against β-actin (A2228; Sigma-Aldrich). Horseradish peroxidase (HRP)-conjugated anti-rabbit IgG (111-035-

144; Jackson ImmunoResearch) was used as a secondary antibody. The HRP-conjugated mouse monoclonal antibody against DDDDK-tag (M185-7; MBL) was used for FLAG tag detection. Immobilon Western Chemiluminescent HRP Substrate (P90715; EMD Millipore) was used to visualize the signals detected by an image analyzer (ImageQuant LAS 4000; Cytiva). Fiji software (ImageJ; National Institutes of Health) was used to adjust contrast and brightness and quantify the signals (Schindelin, Arganda-Carreras et al., 2012).

Immunoprecipitation

Cells were lysed with 1% 3-[(3-cholamidopropyl)-dimethylammonium]-1-propanesulfonate (CHAPS) in lysis buffer and centrifuged at 20,000 g for 15 min. The supernatants were incubated with anti-FLAG M2 affinity gel (A2220; Sigma-Aldrich) for 1 h at 4°C with gentle rotation. The beads were washed three times in washing buffer (20 mM Tris-HCl, pH 8.0, 150 mM NaCl, 1 mM EDTA, and 0.5% CHAPS), and the proteins were eluted with the SDS-PAGE sample buffer.

Immunostaining and fluorescence microscopy

Cells were grown on segmented cover glass (SCC-002; Matsunami Glass IND.), washed with PBS, and fixed with 4% paraformaldehyde (163-20145; Fujifilm Wako Pure Chemical Corporation) in PBS for 10 min. The cells were permeabilized with 50 μg/ml digitonin in PBS for 5 min and blocked with 3% BSA in PBS for 30 min. Primary antibodies in PBS and 3% BSA were added, and samples were incubated for 1 h at room temperature. Cells were washed five times with PBS, incubated with secondary antibodies in PBS with 3% BSA for 1 h at room temperature, and washed five times with PBS. Rabbit polyclonal antibodies against FIP200 (17250-1-AP; ProteinTech) and mouse monoclonal antibodies against FLAG (F1804; Sigma-Aldrich) were used as primary antibodies for immunostaining. Alexa Fluor 488-conjugated anti-mouse IgG (also cross-adsorbed to rabbit IgG and rat IgG) (A-11029; Thermo Fisher Scientific) and Alexa Fluor 555-conjugated anti-rabbit IgG (also cross-adsorbed to mouse IgG) (A-31572; Thermo Fisher Scientific) were used as secondary antibodies. Cells were observed under a confocal microscope (ECLIPSE Ti2; Nikon).

Halo-LC3 processing assay

Cells were treated with 100 nM tetramethylrhodamine (TMR)-conjugated HaloTag ligand (G8251, Promega) for 15 min. After washing twice with PBS, cells were cultured in the starvation medium for 1 h and lysed as described above. Proteins were separated by SDS-PAGE, and in-gel TMR fluorescence was detected using a fluorescent imaging system (Odyssey M; Li-COR).

Statistical analysis

GraphPad Prism 9 software (GraphPad Software) was used for statistical analyses. The statistical methods are described in each figure legend.

Data availability

All the data underlying this study are available in the published article and its online supplemental material.

Acknowledgments

We would like to thank Craig B. Thompson for providing the *Ulk1/2* DKO MEFs; Shoji Yamaoka for the pMRXIP plasmid; Teruhito Yasui for the pCG-gag-pol and pCG-VSV-G plasmids; Sekiko Kurazono and Elijah William Caldwell for assistance with protein preparation. This work was supported in part by JSPS KAKENHI Grant Number JP19H05707, JP23K20044, JP23K06667, JP24H00060 (to NNN), JP23K14140, JP22KJ0044 (to Y.H.), JP21H05731, JP23H02429, JP23K27122, JP23H04923 (to Y.F.), JP21H05256 (to H.Y.), JP22H04919 (to NM), CREST, Japan Science and Technology Agency Grant number JPMJCR20E3 (to NNN), ERATO, Japan Science and Technology Agency Grant number JPMJER1702 (to NM), PRIME, Japan Agency for Medical Research and Development Grant number JP20gm6410009 (to YF), and grants from the Takeda Science Foundation (to NNN, YF).

Disclosures: The authors declare no competing interests exist.

Figure Legends

Figure 1. Structural basis of the ATG13–FIP200 interaction. (A) Structure of the ULK1–ATG13–FIP200 core complex predicted by AlphaFold2. Flexible loop regions in FIP200 were removed from the Figure for clarity. N and C indicate N- and C-terminal regions, respectively. **(B)** Close-up view of the interactions between ATG13 and FIP200. The bottom panels represent the surface model of FIP200 with the coloring based on the electrostatic potentials (blue and red indicate positive and negative potentials, respectively). **(C)** ITC results obtained by titration of MBP-ATG13 (363–517 aa) WT or FIP3A mutant into an FIP200 (1–634 aa) solution. **(D)** Effect of the ATG13 FIP3A mutation on the FIP200 interaction in vivo. *atg13* KO HeLa cells stably expressing FLAG-tagged ATG13 WT or FIP3A were immunoprecipitated with an anti-FLAG antibody and detected with anti-FIP200, anti-ULK1, and anti-FLAG antibodies. **(E)** Relative amounts of precipitated FIP200 in (D) were calculated. Solid bars

indicate the means, and dots indicate the data from three independent experiments. Differences were statistically analyzed using Tukey's multiple comparisons test.

Figure 2. Structural basis of the ULK1–ATG13 interaction. (A) Structure of the ULK1–ATG13 moiety of the ULK1–ATG13–FIP200 core complex in Fig. 1 A (left) and crystal structure of the yeast Atg1–Atg13 complex (right, PDB 4P1N). **(B)** Close-up view of the interactions between $ATG13^{MIM(N)}$ and $ULK1^{MIT2}$ (left) and between $ATG13^{MIM(C)}$ and $ULK1^{MIT1}$ (right). **(C)** ITC results obtained by titration of MBP-ULK1 (636–1050 aa) into a solution of WT or ULK2A mutant of MBP-ATG13 (363–517 aa). Due to weak binding, the K_D value for the ULK2A mutant was not accurately determined. **(D)** Effect of the ATG13-FIP3A mutation on endogenous ULK1 levels in vivo. WT or *atg13* KO HeLa cells stably expressing FLAG-tagged ATG13 WT or ULK2A mutant were lysed, and indicated proteins were detected by immunoblotting using anti-FIP200, anti-ULK1, and anti-FLAG antibodies. **(E)** Relative amounts of ULK1 in (D) were normalized with β-actin and calculated. Solid bars indicate the means, and dots indicate the data from three independent experiments. Differences were statistically analyzed using Tukey's multiple comparisons test.

Figure 3. Structural basis of the ULK1–FIP200 interaction. (A) Structure of the ULK1–FIP200 moiety of the ULK1–ATG13–FIP200 core complex in Fig. 1 A. The right panel represents the surface model of FIP200 with coloring based on the electrostatic potentials (blue and red indicate positive and negative potentials, respectively). Dotted squares indicate the regions displayed in (B). **(B)** Close-up view of the interactions between $ULK1^{MIT1}$ and FIP200 (left) and between $ULK1^{MIT2}$ and FIP200 (right).
(C) In vitro pulldown assay between GST-ULK1 (636–1050 aa) WT or FIP2A mutant with MBP-FIP200 (1–634 aa). **(D)** Relative amounts of precipitated MBP-FIP200 in (C) were calculated. Solid bars indicate the means, and dots indicate the data from three independent experiments. Differences were statistically analyzed using Tukey's multiple comparisons test.
(E) Effect of the ULK1 FIP2A mutation on the FIP200 interaction in vivo. *Ulk1,2* DKO MEFs stably expressing FLAG-tagged ULK1 WT or FIP2A mutant were immunoprecipitated with an anti-FLAG antibody and detected with anti-FIP200, anti-ATG13, and anti-FLAG antibodies.
(F) Relative amounts of precipitated FIP200 (left) and ATG13 (right) in (E) were calculated. Solid bars indicate the means, and dots indicate the data from three independent experiments. Differences were statistically analyzed using Tukey's multiple comparisons test.
(G) Halo-LC3 processing assay of ULK1 FIP2A-expressing cells. *Ulk1,2* DKO MEFs stably expressing Halo-LC3 and FLAG-tagged ULK1 WT or FIP2A mutant were labeled for 15 min with 100 nm TMR-conjugated Halo ligand and incubated in starvation medium for 1 h. Cell

lysates were subjected to in-gel fluorescence detection. **(H)** Halo processing rate in (G). The band intensity of processed Halo and Halo-LC3 in each cell line was quantified, and the relative cleavage rate was calculated as FLAG-ULK1 WT-expressing cells as 1. Solid bars indicate the means, and dots indicate the data from three independent experiments. Data were statistically analyzed using Tukey's multiple comparisons test. **(I)** Colocalization of FLAG-ULK1 WT or FIP2A mutant with FIP200. *Ulk1,2* DKO MEFs stably expressing FLAG-tagged ULK1 WT or FIP2A mutant were immunostained with anti-FLAG and anti-FIP200 antibodies. Scale bar, 10 μm.

Figure 4. ATG13–ULK1 and ATG13–FIP200 interactions complement each other in autophagy function. (A) Schematic representation of the CRISPR-Cas9-mediated KI strategy of ATG13 mutations with FLAG tag. The C-terminally FLAG-tagged coding sequence after the exon 14 of ATG13 with or without FIP3A, ULK2A, or FU5A mutations were knocked in exon 14 of the *Homo sapiens ATG13* locus. As the KI cassette expresses NeoR under the hPGK1 promoter, clones that were successfully knocked in were selected by G418. Cas9-gRNA-targeted sites in the exon 14 of *H. sapiens ATG13* locus are displayed in dark blue. The homology arm for KI is presented in magenta, and the ATG13 CDS and mutations in red and cyan, respectively. NeoR is displayed in brown. Scale bar, 0.5 kilobase pair (kb). **(B)** Immunoblot of ATG13-FLAG KI cell lines. WT, *atg13* KO, and indicated KI HeLa cells were lysed, and indicated proteins were detected by immunoblotting using anti-FIP200, anti-ULK1, and anti-FLAG antibodies. **(C)** Colocalization of endogenous levels of ATG13-FLAG mutants with FIP200. Indicated KI cell lines were cultured in the starvation medium for 1 h and immunostained with anti-FLAG and anti-FIP200 antibodies. Scale bar, 10 μm. **(D)** Halo-LC3 processing assay of ATG13-FLAG KI cell lines. Indicated KI cell lines were labeled for 15 min with 100 nm TMR-conjugated Halo ligand and incubated in starvation medium for 1 h. Cell lysates were subjected to in-gel fluorescence detection. **(E)** Halo processing rate in (D). The band intensity of processed Halo and Halo-LC3 in each cell line was quantified, and the relative cleavage rate was calculated as FLAG-ULK1 WT-expressing cells as 1. Solid bars indicate the means, and dots indicate the data from three independent experiments. Data were statistically analyzed using Tukey's multiple comparisons test. **(F)** Schematic depiction of the difference between the mammalian ULK complex and the yeast Atg1 complex. Mammalian ATG13 binds to two FIP200s within the same FIP200 dimer, contributing to the stability of one ULK1 complex. Conversely, budding yeast Atg13 binds to two Atg17s within a different Atg17 dimer, allowing for endlessly repeated Atg13-Atg17 interactions. ATG101 in the ULK1 complex and Atg31-29 in the Atg1 complex are omitted for simplicity. ATG13/Atg13 is shown in yellow, ULK1/Atg1 in magenta, and FIP200/Atg17 in green. Black lines represent

interactions.

Figure S1. AlphaFold2 prediction of the ULK1–ATG13–FIP200 core complex. (A) Structure of the ULK1–ATG13–FIP200 core complex with flexible loops omitted from Fig. 1 A. **(B)** The structure in (A) is colored based on the pLDDT values.

Figure S2. SDS-PAGE of recombinant proteins used for ITC and in vitro pull-down experiments. Protein bands were stained with Coomassie Brilliant Blue.

Figure S3. Stable overexpression of *ATG13* results in 10-fold higher protein expression than the endogenous version.
(A) Comparison of *ATG13* expression level. WT, *atg13* KO stably expressing ATG13-FLAG, and ATG13-FLAG KI HeLa cells were lysed, and indicated proteins were detected by immunoblotting using anti-ATG13, anti-FIP200, anti-ULK1, and anti-β-actin antibodies. **(B)** Relative amounts of ATG13 in (A) were calculated as WT HeLa cells as 1. Solid bars indicate the means, and dots indicate the data from three independent experiments. Differences were statistically analyzed using Tukey's multiple comparisons test.

References

Alers S, Loffler AS, Paasch F, Dieterle AM, Keppeler H, Lauber K, Campbell DG, Fehrenbacher B, Schaller M, Wesselborg S, Stork B. 2011. Atg13 and FIP200 act independently of Ulk1 and Ulk2 in autophagy induction. *Autophagy* **7**:1423-1433. doi: 10.4161/auto.7.12.18027.

Alers S, Wesselborg S, Stork B. 2014. ATG13: just a companion, or an executor of the autophagic program? *Autophagy* **10**:944-956. doi: 10.4161/auto.28987.

Burki F, Roger AJ, Brown MW, Simpson AGB. 2020. The New Tree of Eukaryotes. *Trends Ecol Evol* **35**:43-55. doi: 10.1016/j.tree.2019.08.008.

Cheong H, Lindsten T, Wu J, Lu C, Thompson CB. 2011. Ammonia-induced autophagy is independent of ULK1/ULK2 kinases. *Proc Natl Acad Sci U S A* **108**:11121-11126. doi: 10.1073/pnas.1107969108.

Evans R, O'Neill M, Pritzel A, Antropova N, Senior A, Green T, Žídek A, Bates R, Blackwell S, Yim J, Ronneberger O, Bodenstein S, Zielinski M, Bridgland A, Potapenko A, Cowie A, Tunyasuvunakool K, Jain R, Clancy E, Kohli P et al. 2021. Protein complex prediction with AlphaFold-Multimer. *bioRxiv*:2021.2010.2004.463034. doi: 10.1101/2021.10.04.463034.

Fujioka Y, Alam JM, Noshiro D, Mouri K, Ando T, Okada Y, May AI, Knorr RL, Suzuki K, Ohsumi Y, Noda NN. 2020. Phase separation organizes the site of autophagosome formation. *Nature*

578:301-305. doi: 10.1038/s41586-020-1977-6.
Fujioka Y, Suzuki SW, Yamamoto H, Kondo-Kakuta C, Kimura Y, Hirano H, Akada R, Inagaki F, Ohsumi Y, Noda NN. 2014. Structural basis of starvation-induced assembly of the autophagy initiation complex. *Nat Struct Mol Biol* 21:513-521. doi: 10.1038/nsmb.2822.
Ganley IG, Lam du H, Wang J, Ding X, Chen S, Jiang X. 2009. ULK1.ATG13.FIP200 complex mediates mTOR signaling and is essential for autophagy. *J Biol Chem* 284:12297-12305. doi: 10.1074/jbc.M900573200.
Hama Y, Kurikawa Y, Matsui T, Mizushima N, Yamamoto H. 2023. TAX1BP1 recruits ATG9 vesicles through SCAMP3 binding. *bioRxiv*:2023.2008.2018.553817. doi: 10.1101/2023.08.18.553817.
Hieke N, Loffler AS, Kaizuka T, Berleth N, Bohler P, Driessen S, Stuhldreier F, Friesen O, Assani K, Schmitz K, Peter C, Diedrich B, Dengjel J, Holland P, Simonsen A, Wesselborg S, Mizushima N, Stork B. 2015. Expression of a ULK1/2 binding-deficient ATG13 variant can partially restore autophagic activity in ATG13-deficient cells. *Autophagy* 11:1471-1483. doi: 10.1080/15548627.2015.1068488.
Hosokawa N, Hara T, Kaizuka T, Kishi C, Takamura A, Miura Y, Iemura S, Natsume T, Takehana K, Yamada N, Guan JL, Oshiro N, Mizushima N. 2009. Nutrient-dependent mTORC1 association with the ULK1-Atg13-FIP200 complex required for autophagy. *Mol Biol Cell* 20:1981-1991. doi: 10.1091/mbc.e08-12-1248.
Jung CH, Jun CB, Ro SH, Kim YM, Otto NM, Cao J, Kundu M, Kim DH. 2009. ULK-Atg13-FIP200 complexes mediate mTOR signaling to the autophagy machinery. *Mol Biol Cell* 20:1992-2003. doi: 10.1091/mbc.e08-12-1249.
Kannangara AR, Poole DM, McEwan CM, Youngs JC, Weerasekara VK, Thornock AM, Lazaro MT, Balasooriya ER, Oh LM, Soderblom EJ, Lee JJ, Simmons DL, Andersen JL. 2021. BioID reveals an ATG9A interaction with ATG13-ATG101 in the degradation of p62/SQSTM1-ubiquitin clusters. *EMBO Rep* 22:e51136. doi: 10.15252/embr.202051136.
Kim J, Kamada Y, Stromhaug PE, Guan J, Hefner-Gravink A, Baba M, Scott SV, Ohsumi Y, Dunn WA, Jr., Klionsky DJ. 2001. Cvt9/Gsa9 functions in sequestering selective cytosolic cargo destined for the vacuole. *J Cell Biol* 153:381-396. doi: 10.1083/jcb.153.2.381.
Kishi-Itakura C, Koyama-Honda I, Itakura E, Mizushima N. 2014. Ultrastructural analysis of autophagosome organization using mammalian autophagy-deficient cells. *J Cell Sci* 127:4089-4102. doi: 10.1242/jcs.156034.
Kitamura T, Koshino Y, Shibata F, Oki T, Nakajima H, Nosaka T, Kumagai H. 2003. Retrovirus-mediated gene transfer and expression cloning: powerful tools in functional genomics. *Exp Hematol* 31:1007-1014. doi:
Li F, Chung T, Vierstra RD. 2014. AUTOPHAGY-RELATED11 plays a critical role in general

autophagy- and senescence-induced mitophagy in Arabidopsis. *Plant Cell* **26**:788-807. doi: 10.1105/tpc.113.120014.

Lin MG, Hurley JH. 2016. Structure and function of the ULK1 complex in autophagy. *Curr Opin Cell Biol* **39**:61-68. doi: 10.1016/j.ceb.2016.02.010.

Mizushima N. 2010. The role of the Atg1/ULK1 complex in autophagy regulation. *Curr Opin Cell Biol* **22**:132-139. doi: 10.1016/j.ceb.2009.12.004.

Mizushima N, Komatsu M. 2011. Autophagy: renovation of cells and tissues. *Cell* **147**:728-741. doi: 10.1016/j.cell.2011.10.026.

Mizushima N, Levine B. 2020. Autophagy in Human Diseases. *N Engl J Med* **383**:1564-1576. doi: 10.1056/NEJMra2022774.

Nakatogawa H. 2020. Mechanisms governing autophagosome biogenesis. *Nat Rev Mol Cell Biol* **21**:439-458. doi: 10.1038/s41580-020-0241-0.

Noda NN. 2024. Structural view on autophagosome formation. *FEBS Lett* **598**:84-106. doi: 10.1002/1873-3468.14742.

Pan ZQ, Shao GC, Liu XM, Chen Q, Dong MQ, Du LL. 2020. Atg1 kinase in fission yeast is activated by Atg11-mediated dimerization and cis-autophosphorylation. *Elife* **9**doi: 10.7554/eLife.58073.

Papinski D, Kraft C. 2016. Regulation of Autophagy By Signaling Through the Atg1/ULK1 Complex. *J Mol Biol* **428**:1725-1741. doi: 10.1016/j.jmb.2016.03.030.

Ragusa MJ, Stanley RE, Hurley JH. 2012. Architecture of the Atg17 complex as a scaffold for autophagosome biogenesis. *Cell* **151**:1501-1512. doi: 10.1016/j.cell.2012.11.028.

Ren X, Nguyen TN, Lam WK, Buffalo CZ, Lazarou M, Yokom AL, Hurley JH. 2023. Structural basis for ATG9A recruitment to the ULK1 complex in mitophagy initiation. *Sci Adv* **9**:eadg2997. doi: 10.1126/sciadv.adg2997.

Rudinskiy M, Bergmann TJ, Molinari M. 2022. Quantitative and time-resolved monitoring of organelle and protein delivery to the lysosome with a tandem fluorescent Halo-GFP reporter. *Mol Biol Cell* **33**:ar57. doi: 10.1091/mbc.E21-10-0526.

Saitoh T, Nakayama M, Nakano H, Yagita H, Yamamoto N, Yamaoka S. 2003. TWEAK induces NF-kappaB2 p100 processing and long lasting NF-kappaB activation. *J Biol Chem* **278**:36005-36012. doi: 10.1074/jbc.M304266200.

Schindelin J, Arganda-Carreras I, Frise E, Kaynig V, Longair M, Pietzsch T, Preibisch S, Rueden C, Saalfeld S, Schmid B, Tinevez JY, White DJ, Hartenstein V, Eliceiri K, Tomancak P, Cardona A. 2012. Fiji: an open-source platform for biological-image analysis. *Nat Methods* **9**:676-682. doi: 10.1038/nmeth.2019.

Shi X, Yokom AL, Wang C, Young LN, Youle RJ, Hurley JH. 2020. ULK complex organization in autophagy by a C-shaped FIP200 N-terminal domain dimer. *J Cell Biol* **219**doi:

10.1083/jcb.201911047.
Sun LL, Li M, Suo F, Liu XM, Shen EZ, Yang B, Dong MQ, He WZ, Du LL. 2013. Global analysis of fission yeast mating genes reveals new autophagy factors. *PLoS Genet* **9**:e1003715. doi: 10.1371/journal.pgen.1003715.
Suzuki K, Kirisako T, Kamada Y, Mizushima N, Noda T, Ohsumi Y. 2001. The pre-autophagosomal structure organized by concerted functions of APG genes is essential for autophagosome formation. *EMBO J* **20**:5971-5981. doi: 10.1093/emboj/20.21.5971.
Wallot-Hieke N, Verma N, Schlutermann D, Berleth N, Deitersen J, Bohler P, Stuhldreier F, Wu W, Seggewiss S, Peter C, Gohlke H, Mizushima N, Stork B. 2018. Systematic analysis of ATG13 domain requirements for autophagy induction. *Autophagy* **14**:743-763. doi: 10.1080/15548627.2017.1387342.
Wong PM, Puente C, Ganley IG, Jiang X. 2013. The ULK1 complex: sensing nutrient signals for autophagy activation. *Autophagy* **9**:124-137. doi: 10.4161/auto.23323.
Yamamoto H, Fujioka Y, Suzuki SW, Noshiro D, Suzuki H, Kondo-Kakuta C, Kimura Y, Hirano H, Ando T, Noda NN, Ohsumi Y. 2016. The Intrinsically Disordered Protein Atg13 Mediates Supramolecular Assembly of Autophagy Initiation Complexes. *Dev Cell* **38**:86-99. doi: 10.1016/j.devcel.2016.06.015.
Yamamoto H, Kakuta S, Watanabe TM, Kitamura A, Sekito T, Kondo-Kakuta C, Ichikawa R, Kinjo M, Ohsumi Y. 2012. Atg9 vesicles are an important membrane source during early steps of autophagosome formation. *J Cell Biol* **198**:219-233. doi: 10.1083/jcb.201202061.
Yim WW, Yamamoto H, Mizushima N. 2022. A pulse-chasable reporter processing assay for mammalian autophagic flux with HaloTag. *Elife* **11**doi: 10.7554/eLife.78923.
Yorimitsu T, Klionsky DJ. 2005. Atg11 links cargo to the vesicle-forming machinery in the cytoplasm to vacuole targeting pathway. *Mol Biol Cell* **16**:1593-1605. doi: 10.1091/mbc.e04-11-1035.
Zheng Q, Chen Y, Chen D, Zhao H, Feng Y, Meng Q, Zhao Y, Zhang H. 2022. Calcium transients on the ER surface trigger liquid-liquid phase separation of FIP200 to specify autophagosome initiation sites. *Cell* **185**:4082-4098 e4022. doi: 10.1016/j.cell.2022.09.001.
Zhou Z, Liu J, Fu T, Wu P, Peng C, Gong X, Wang Y, Zhang M, Li Y, Wang Y, Xu X, Li M, Pan L. 2021. Phosphorylation regulates the binding of autophagy receptors to FIP200 Claw domain for selective autophagy initiation. *Nat Commun* **12**:1570. doi: 10.1038/s41467-021-21874-1.

Figure 1

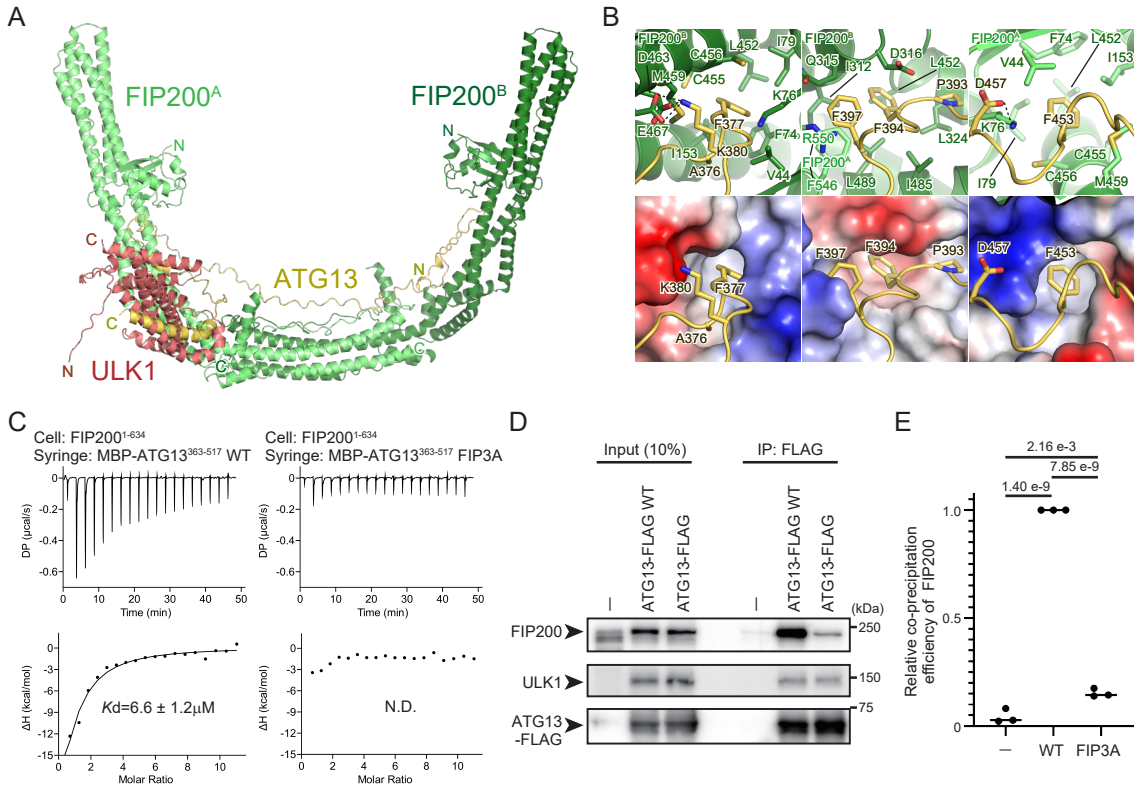
A
FIP200A
FIP200B
ATG13
ULK1
N
C
B
C
Cell: FIP200 1-634
Syringe: MBP-ATG13 363-517 WT
Cell: FIP200 1-634
Syringe: MBP-ATG13 363-517 FIP3A
DP (µcal/s)
Time (min)
ΔH (kcal/mol)
Molar Ratio
Kd=6.6 ± 1.2µM
N.D.
D
Input (10%)
IP: FLAG
ATG13-FLAG WT
ATG13-FLAG
FIP200
ULK1
ATG13 -FLAG
(kDa)
250
150
75
E
2.16 e-3
7.85 e-9
1.40 e-9
Relative co-precipitation efficiency of FIP200
WT
FIP3A

Figure 2

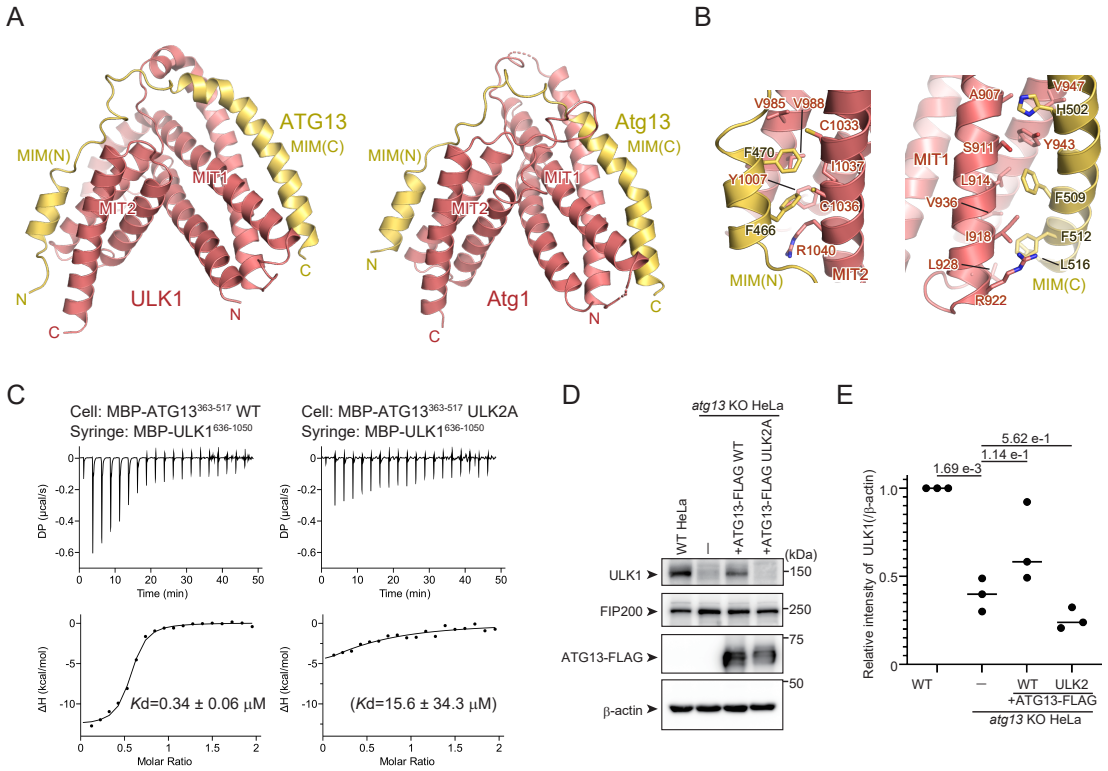
A
ATG13
MIM(C)
MIM(N)
MIT1
MIT2
ULK1
N
C
Atg13
Atg1
B
V985
V988
C1033
F470
I1037
Y1007
C1036
F466
R1040
MIM(N)
MIT2
A907
V947
H502
MIT1
S911
Y943
L914
V936
F509
I918
F512
L928
L516
R922
MIM(C)
C
Cell: MBP-ATG13363-517 WT
Syringe: MBP-ULK1636-1050
Cell: MBP-ATG13363-517 ULK2A
Syringe: MBP-ULK1636-1050
DP (µcal/s)
Time (min)
ΔH (kcal/mol)
Molar Ratio
Kd=0.34 ± 0.06 µM
(Kd=15.6 ± 34.3 µM)
D
atg13 KO HeLa
WT HeLa
–
+ATG13-FLAG WT
+ATG13-FLAG ULK2A
(kDa)
ULK1
FIP200
ATG13-FLAG
β-actin
150
250
75
50
E
5.62 e-1
1.14 e-1
1.69 e-3
Relative intensity of ULK1/(β-actin)
WT
–
WT
ULK2
+ATG13-FLAG
atg13 KO HeLa

Figure 3

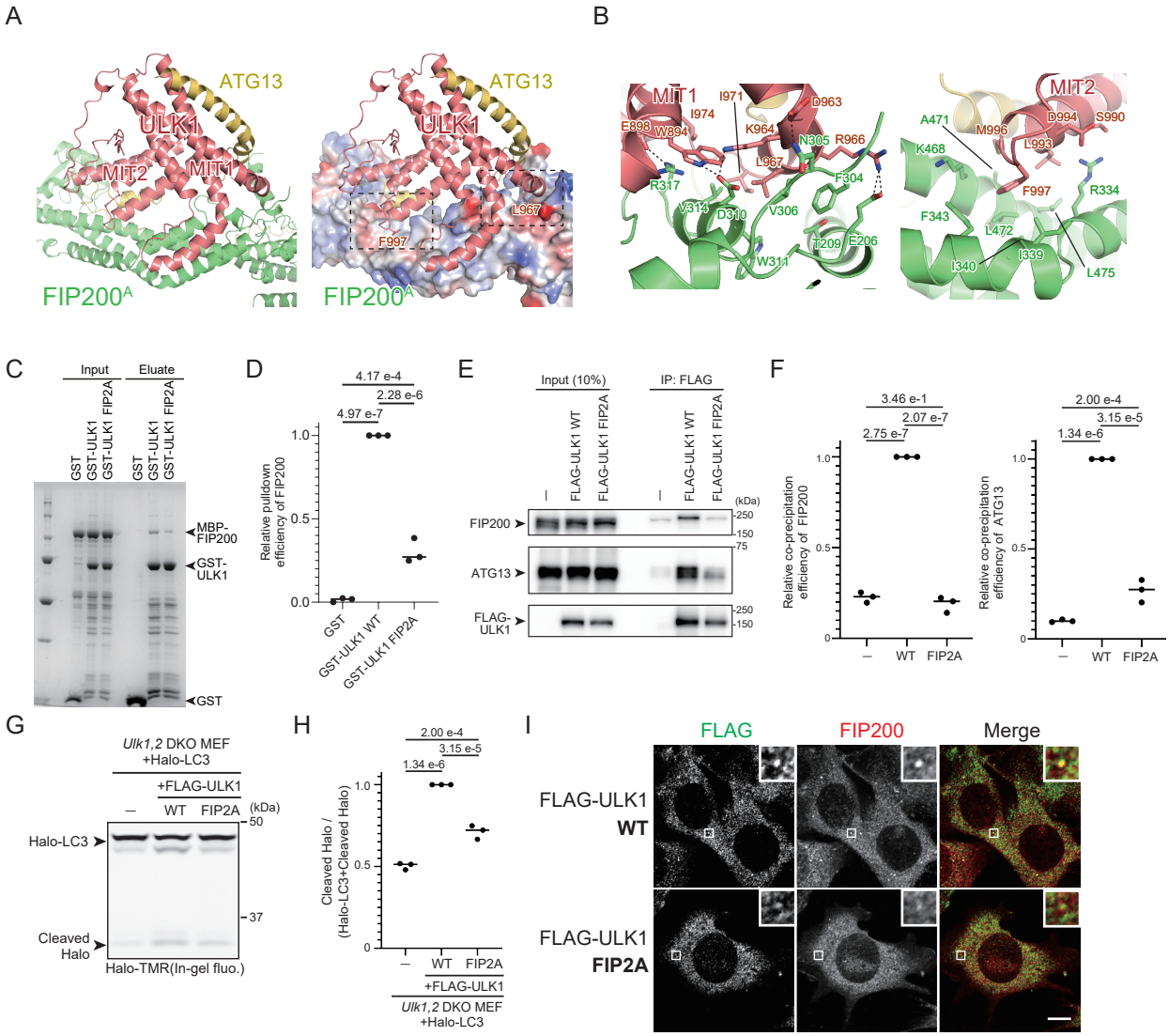
A
ATG13
ULK1
MIT2
MIT1
FIP200A
ATG13
ULK1
F997
L967
FIP200A
B
MIT1
I971
D963
I974
E893
W894
K964
N305
R966
L967
R317
F304
V314
D310
V306
T209
E206
W311
MIT2
A471
M996
D994
S990
L993
K468
F997
R334
F343
L472
I339
I340
L475
C
Input
Eluate
GST
GST-ULK1
GST-ULK1 FIP2A
GST
GST-ULK1
GST-ULK1 FIP2A
MBP-FIP200
GST-ULK1
GST
D
4.17 e-4
2.28 e-6
4.97 e-7
Relative pulldown efficiency of FIP200
1.0
0.5
0.0
GST
GST-ULK1 WT
GST-ULK1 FIP2A
E
Input (10%)
IP: FLAG
–
FLAG-ULK1 WT
FLAG-ULK1 FIP2A
–
FLAG-ULK1 WT
FLAG-ULK1 FIP2A
(kDa)
FIP200
ATG13
FLAG-ULK1
250
150
75
250
150
F
3.46 e-1
2.07 e-7
2.75 e-7
Relative co-precipitation efficiency of FIP200
1.0
0.5
0
–
WT
FIP2A
2.00 e-4
3.15 e-5
1.34 e-6
Relative co-precipitation efficiency of ATG13
1.0
0.5
0
–
WT
FIP2A
G
Ulk1,2 DKO MEF
+Halo-LC3
+FLAG-ULK1
–
WT
FIP2A
(kDa)
Halo-LC3
50
37
Cleaved Halo
Halo-TMR(In-gel fluo.)
H
2.00 e-4
3.15 e-5
1.34 e-6
Cleaved Halo / (Halo-LC3+Cleaved Halo)
1.0
0.5
0
–
WT
FIP2A
+FLAG-ULK1
Ulk1,2 DKO MEF
+Halo-LC3
I
FLAG
FIP200
Merge
FLAG-ULK1
WT
FLAG-ULK1
FIP2A

Figure 4

A

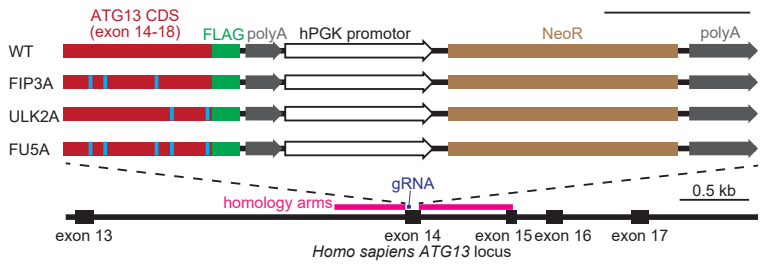

B

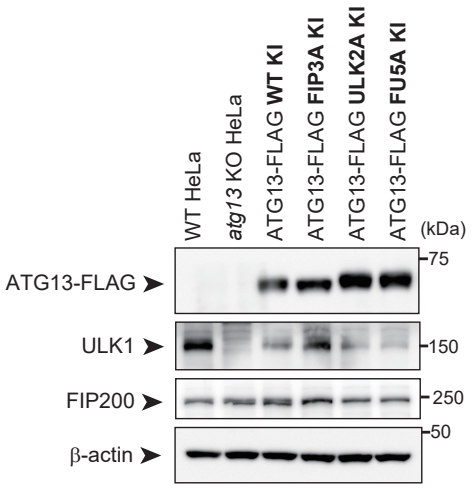

C

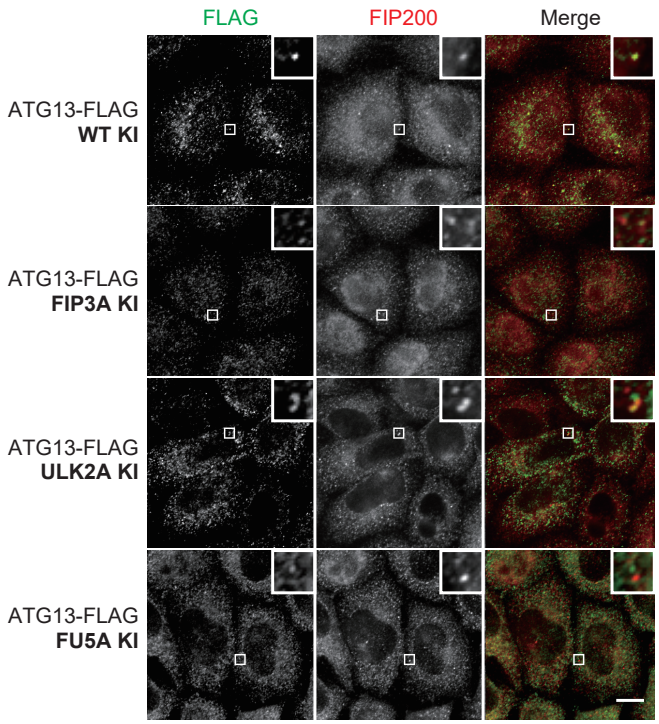

D

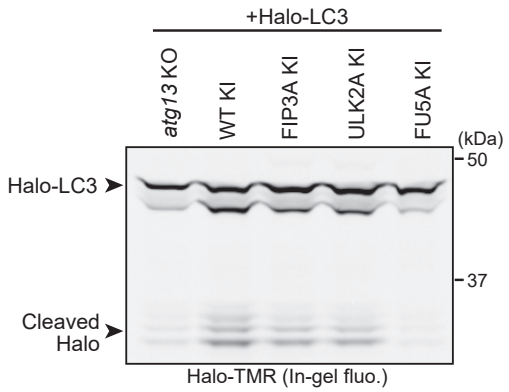

E

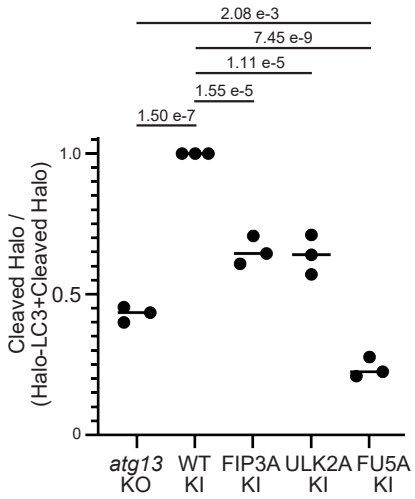
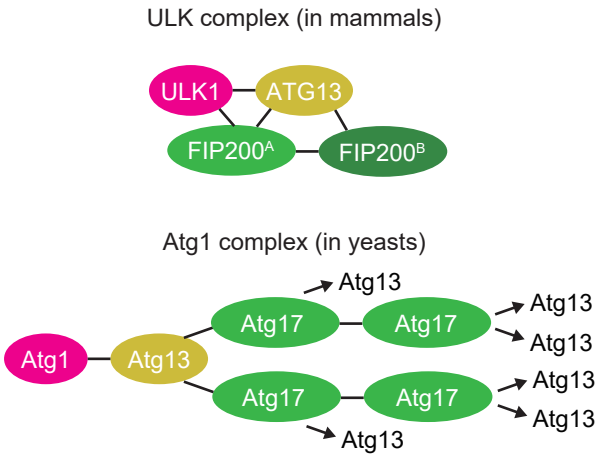
F